



Uncovering Heterogeneity in Alzheimer's Disease from Graphical Modeling of the Tau Spatiotemporal Topography

Jiaxin Yue^{1,2} and Yonggang Shi^{1,2}(✉)

¹ Stevens Neuroimaging and Informatics Institute, Keck School of Medicine, University of Southern California (USC), Los Angeles, CA 90033, USA
yonggans@usc.edu

² Ming Hsieh Department of Electrical and Computer Engineering, Viterbi School of Engineering, University of Southern California (USC), Los Angeles, CA 90089, USA

Abstract. Growing evidence from post-mortem and in vivo studies have demonstrated the substantial variability of tau pathology spreading patterns in Alzheimer's disease (AD). Automated tools for characterizing the heterogeneity of tau pathology will enable a more accurate understanding of the disease and help the development of targeted treatment. In this paper, we propose a Reeb graph representation of tau pathology topography on cortical surfaces using tau PET imaging data. By comparing the spatial and temporal coherence of the Reeb graph representation across subjects, we can build a directed graph to represent the distribution of tau topography over a population, which naturally facilitates the discovery of spatiotemporal subtypes of tau pathology with graph-based clustering. In our experiments, we conducted extensive comparisons with state-of-the-art event-based model on synthetic and large-scale tau PET imaging data from ADNI3 and A4 studies. We demonstrated that our proposed method can more robustly achieve the subtyping of tau pathology with clear clinical significance and demonstrated superior generalization performance than event-based model.

Keywords: Heterogeneity · Tau pathology · Reeb graph

1 Introduction

With emerging evidence from various post-mortem and in vivo tau PET imaging studies, the existence of several well-recognized atypical patterns of neurofibrillary tangle distribution in subsets of patients and abnormal clinical presentations challenge [4] the notion that tau pathology follows a uniform Braak-like progression throughout the brain in Alzheimer's disease (AD) [2]. Disentangling tau pathology heterogeneity can thus greatly contribute to develop more accurate diagnosis, prognosis and targeted treatment for AD.

This work is supported by the National Institute of Health (NIH) under grants R01EB022744, RF1AG077578, RF1AG056573, RF1AG064584, R21AG064776, P41EB015922, U19AG078109.

© The Author(s), under exclusive license to Springer Nature Switzerland AG 2023
H. Greenspan et al. (Eds.): MICCAI 2023, LNCS 14224, pp. 262–271, 2023.
https://doi.org/10.1007/978-3-031-43904-9_26

In contrast to many previous studies [7, 14, 16] utilizing clustering methods based on spatial variants for subtyping, spatiotemporal methods have recently gained popularity, combining spatial patterns and disease staging in a single framework. Event-based model [5, 17] is a state-of-art spatiotemporal method that requires only cross-sectional data to automatically detect multiple spatiotemporal trajectories. However, the trajectory depends on the biomarker selection, and the predefined region-of-interest (ROI) based parcellations ignore the regional relations and the topological changes of pathology within the brain. Besides, the method focuses more on temporal transitions but neglects regional coherence. Moreover, the estimation requires large sample sizes to cover enough phenotype and intensity variants for better model fitting.

To address these limitations, this paper presents a novel Reeb graph representation that encodes the topography of tau pathology from PET imaging, and a directed-graph-based framework for uncovering spatiotemporal heterogeneity from cross-sectional tau PET data. More specifically, we first generate a pattern representation from Reeb graph analysis on cortical surfaces to encode the tau pathology pattern. Secondly, the spatial coherence and temporal consistency of tau spreading patterns across subjects are combined within a directed graph for clustering, which is robust to sample sizes and intensity deviations. With large-scale imaging data from the ADNI and A4 studies, we obtained three subtypes with systematic spatiotemporal variations in tau spreading patterns by utilizing an efficient community detection method on graphs. We also demonstrate that our method exhibits more robust generalization performance than event-based model on both synthetic and real data.

2 Method

2.1 Reeb Graph Analysis for Pathology Detection

The reeb graph encodes the topology of pathology on the cortical surface and is used to extract the salient tau pathological patterns. Given a Morse function f on the mesh \mathcal{M} , its Reeb graph is defined as follows [10]:

Definition 1. *Let $f : \mathcal{M} \rightarrow \mathbb{R}$. The Reeb graph $R(f)$ of f is the quotient space with its topology defined through the equivalent relation $x \simeq y$ if $f(x) = f(y)$ for $\forall x, y \in \mathcal{M}$.*

In our work, \mathcal{M} is a common template surface *fsaverage* from FreeSurfer [6], and f is the tau standardized uptake value ratio (SUVR) map defined on \mathcal{M} . For numerical calculation of the Reeb graph of f on \mathcal{M} , we use the algorithm proposed in [11]. Because the topology only changes at critical points (minimum, maximum and saddle points), for a given SUVR map f on cortical surface \mathcal{M} , we first sort its critical points $C = \{C_1, C_2, \dots, C_K\}$ according to their SUVR values such that $f(C_1) < f(C_2) < \dots < f(C_K)$. The surface can be partitioned by using the level contours in the neighborhood of these critical points, and the neighboring nodes are connected in the Reeb graph through arcs by applying

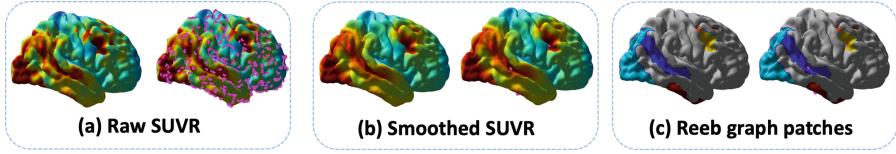


Fig. 1. Reeb graph simplification. (a) The Reeb graph of the original SUVR function is dominated by a large number of noisy peaks (purple points). (b) After graph simplification, the number of peaks (purple points) is significantly reduced. (c) Reeb graph patches can encode the salient tau pathology patterns. (color figure online)

region growing. The generated Reeb graph is represented as $R(f) = (C, E)$, where C is the nodes of the graph, and E is the edges of the graph.

We further develop a Reeb graph simplification scheme to remove the noisy peaks of the original SUVR function (Fig. 1(a)) for salient pattern detection. Firstly, we iteratively apply Laplacian smoothing on an SUVR map until the Reeb graph reaches a common level of complexity, which is measured as the number of nodes in the graph. Then we use a Reeb graph simplification algorithm [12] to merge nodes around saddle points based on their persistence. For an edge $E_k = (C_i, C_j) (f(C_j) > f(C_i))$ of the Reeb graph $R(f) = (C, E)$, its weight is defined according to its persistence:

$$w(E_k) = A_k \times f(C_j) \quad (1)$$

where A_k is area of the patch enclosed by triangles belonging to this edge, and $f(C_j)$ is the peak SUVR value of this patch. To simplify the Reeb graph, we iteratively remove saddle points and spurious edges based on the persistence threshold δ . At each iteration, we scan these saddle points sequentially and for an edge $E_k = (C_i, C_j) (f(C_i) < f(C_j))$ with $w(E_k) > \delta$, we collapse this edge by removing C_i and adding all its connections to C_j . The weights of these new edges are updated according to Eq. 1. These steps can be repeated until the persistent threshold is reached. The pruned Reeb graph is illustrated in Fig. 1(c). The number of critical points in the pruned Reeb graph is determined by the complexity of SUVR function and the persistence threshold. We set $\delta = 300$ so the pruned Reeb graph typically has less than 10 patches. The edges of the simplified Reeb graph are sets of triangles with topological changes, and the patches enclosed by these triangle sets are the regions with salient tau pathology.

2.2 Directed Graph Construction for Spatiotemporal Subtyping

The Reeb graph patches of different subjects typically have distinct shapes, which makes patch matching an essential step for pattern comparison. The solution we develop here is to establish patch correspondence between subjects based on their spatial proximity by an assignment algorithm. We define the cost function for matching the patch x_i of subject x and the patch y_j of subject y as:

$$C_{x_i, y_j} = dPeak_{x_i, y_j} \times dHausdorff_{x_i, y_j} \quad (2)$$

where $dPeak$ is the distance between the peaks, and $dHausdorff$ is the Hausdorff distance between two patch sets. Both are calculated based on geodesic distances on the surface.

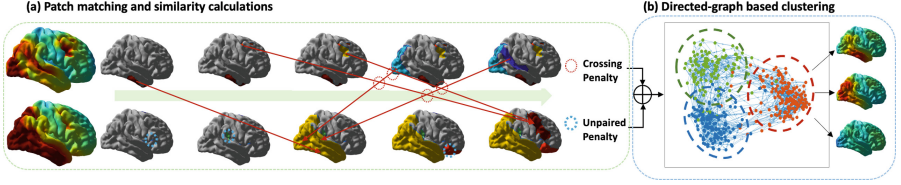


Fig. 2. Directed graph construction for clustering. (a) Patch matching and similarity calculations. The patches are arranged in a peak SUVR value decreasing order, so from left to right, the sequence shows the pathology accumulation process. The spatial approximate correspondences are linked by the red arrows, and the temporal inconsistency is highlighted by red circles. The unpaired patches are highlighted by blue circles. (b) Visualization of directed graph and graph-based clustering. (Color figure online)

Patch matching is achieved through iterative assignments to accommodate both one-to-one and many-to-one matching. The latter one is illustrated in Fig. 2(a) that multiple small patches have the same correspondences. At iteration t , a cost function C_t is calculated for the unpaired patches in x and all patches in the reference subject y . A linear assignment [3] is applied with the cost function C_t and the unpaired cost c_t to establish the one-to-one correspondences and add it into the correspondence set Φ . The iterations repeat until $\min(C_t) > c_t$, and the resulting correspondences represent patches with spatial proximity across subjects.

The spatiotemporal similarity of tau pathology implies spatial coherence and temporal consistency, and the directed graph can be used to encode both the similarity as the edge weight and the disease staging as edge direction. The temporal similarity is derived from the consistency of the pathology occurring orders based on the correspondences. Based on the assumption that tau accumulation is a monotonic process, we sort the Reeb graph patches y_i in a peak SUVR descending order, and this sequence implies the patch occurring order. When comparing with subject x , patches x_i are arranged according to their correspondences y_i . For patches of x having the same correspondence in y , they are sorted based on their own peak SUVR values decreasingly. The temporal crossings between the two sequences as indicated in Fig. 2(a) imply the existence of temporal inconsistency between the two SUVR maps. A crossing penalty is then defined to quantify this inconsistency:

$$D_{crossing_{x,y}} = \sum_{x_i} \sum_{x_j, \forall j > i} \max(0, SUVR_{x_j} - SUVR_{x_i}) \times PatchS_{x_i}, \quad (3)$$

$$SUVR_{y_i} > SUVR_{y_j} \text{ for } i < j$$

where $SUVR_{x_i}$ is the peak SUVR of x_i , and $PatchS_{x_i}$ is the patch size.

The spatial coherence can be estimated from the spatial deviations caused by the unpaired patches. An unpaired penalty is defined as:

$$Dunpair_{x,y} = \sum_{x_i} \frac{SUVR_{x_i}}{\max_{x_i} SUVR_{x_i}} \times PatchS_{x_i} \times \mathbf{I}_i, \mathbf{I}_i = \begin{cases} 0 & \text{if } x_i \in \Phi \\ 1 & \text{if } x_i \notin \Phi \end{cases} \quad (4)$$

The crossing and unpaired penalties are combined to define a distance matrix:

$$D_{x,y} = \alpha \times D_{crossing_{x,y}} + \beta \times Dunpair_{x,y} \quad (5)$$

where D is weighted combination of two penaty terms by α and β . For the construction of a dense graph, we transform D into a similarity matrix $S = 1/(1 + D)$ as the weights between each pair of subjects. To maintain sparsity and form clusters, we primarily focus on subjects exhibiting similar patterns and adopt a K-nearest-neighbor(KNN) approach to keep only the top K-relevant connections for each subject.

Disease staging is determined based on the assumption that later-stage subjects typically have more widespread distribution of tau pathology and/or higher peak intensities. To generate directionality between subjects in our graph representation, we calculate an unnormalized unpaired penalty as $Dun\tilde{pair}_{x,y} = Dunpair_{x,y} \times \max_{x_i} SUVR_{x_i}$ because it is composed of both the spreading size and SUVR values. Specifically, if $Dun\tilde{pair}_{x,y} > Dun\tilde{pair}_{y,x}$, then subject x is considered to be in a later stage than y because of having more tau pathology and higher SUVR values, so the edge direction is $y \rightarrow x$. By applying the directions to the KNN graph, we get a directed graph for representing the spatiotemporal relationships between subjects as illustrated in Fig. 2(b). For the subtyping of tau spatiotemporal topography, the Louvain community detection method [1] is applied for clustering on the directed graph by maximizing modularity. The modularity is high when the intra-subtype connections are dense while the inter-subtype connections are sparse.

3 Experiments and Results

In the current work, we choose the unpaired costs $c_1 = 300$ and $c_i = 500(i > 1)$ in linear assignment of patches, the weights for distance matrix definition as $\alpha = 2$ and $\beta = 1$, and $K = 10$ for KNN-based graph construction. For Louvain community detection on directed graphs, we set its resolution parameter $\gamma = 0.3$. Beside clustering based on the directed graph from training data, we can apply the trained model from our method to estimate the subtype of a validation/test set via major voting by the K most similar training samples.

For the event-based SuStaIn method [17], the same experimental settings in [15] were used. The SUVR values are first normalized based on the normal control samples to create the tau z-scores. We used the z-score of 5 ROIs (parietal, frontal, occipital, temporal, and medial temporal lobe) and cut-off thresholds of $z = 2, 5$ and 10 for event definition. To apply the trained model to a validation/test data, we obtain subtype membership by fitting the new subject into the pre-trained SuStaIn model.

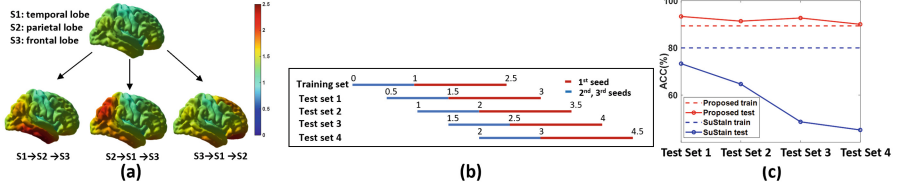


Fig. 3. Synthetic data and results. (a) Average SUVR maps of three subtypes. Each subtype has a distinct tau propagation trajectory from three seed regions (S1, S2, S3). (b) The magnitude ranges of seeds for all datasets. (c) The clustering performance on training and four test sets.

3.1 Synthetic Experiments

Synthetic Data. The synthetic tau SUVR data is generated by adding simulated values derived from a Gaussian mixture model to an SUVR template ($SUVR_{tem}$), which is calculated as the mean of normal controls, as follows:

$$SUVR = SUVR_{tem} + \sum_{k=1,2,3} f(\mathbf{x}_k|0, \sigma) \times a_k \quad (6)$$

where f is a Gaussian distribution, \mathbf{x}_k is the distance vector to seed k , and the standard deviation σ measures the spreading size. The magnitudes of the seeds a_k are sampled from the ranges shown in Fig. 3(b). A training set and four test sets with different magnitude ranges and seeds randomly sampled from temporal, parietal and frontal lobe, respectively, were generated. Each set has three subtypes with distinct tau propagation orders as shown in Fig. 3(a), and each subtype contains 50 samples.

Synthetic Results. The performances are measured by accuracy and shown in Fig. 3. First, our method (89.33%) achieved better performance over the SuStain method (80%) on training set. Second, we applied the trained model of both methods to the four test sets and results are shown in Fig. 3(c). With the increasing difference between the test and training set, performance of the SuStain method decreases quite significantly while our method maintains a stable performance. This shows the robustness of our method with respect to intensity changes from the training to the testing set and potentially better generalization ability as we will further demonstrate next in real data experiments.

3.2 Real Data Experiments

Real Dataset. 706 tau PET scans from Alzheimer’s Disease Neuroimaging Initiative (ADNI) (adni.loni.usc.edu) and Anti-Amyloid Treatment in Asymptomatic Alzheimer’s (A4) [13] are used. 427 amyloid-positive-tau-positive (A+T+) images are used for subtyping analysis. A+/A- labels were provided by the ADNI and A4 study, T+/T- status was defined if the image with peak

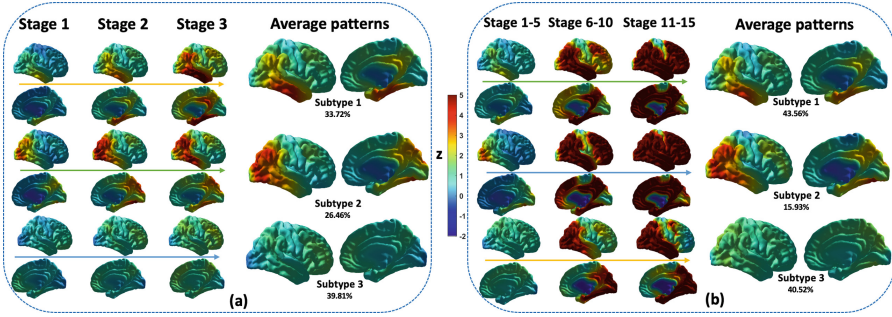


Fig. 4. Subtyping results on A+T+ subjects. (a) Patterns of three subtypes uncovered by our method. (b) Patterns of three subtypes uncovered by the SuStaIn method. 15 stages of the SuStaIn method are merged into 3 stages for comparison.

SUVR value exceeding 1.5 [9]. Besides, 279 cognitively normal A-T- subjects were selected as normal controls. The demographic information of the cohorts are listed in Table 1. All tau PET images were averaged across frames and registered to individual T1 space to obtain the skull-stripped images. Besides, T1 images were preprocessed using Freesurfer [6] to get their volume parcellation using the Desikan-Killiany atlas. The registered tau PET images were intensity-normalized using an inferior cerebellar gray matter reference region, resulting in SUVR images.

Subtyping A+T+ Subjects. Using A+T+ data, we obtained three pathologically different subtypes for both methods (Fig. 4). In our method, the staging was derived from the degree of the nodes in the dense directed graph as $d_i = indegree_i - outdegree_i$. Two thresholds (-50 and 50) were set as the cut-offs to define three stages for each subtype. For subtype 1, more tau pathology distributes in the temporal lobe, and its propagation is consistent with the classic Braak staging [2]; for subtype 2, tau pathology primarily occurs in the occipital area and sequentially spreads to parietal and other regions; subtype 3 does not show significant differences among brain regions, and the overall SUVR is lower among all subtypes. For both methods, the average patterns are similar in three subtypes. However, comparing across stages, the intensities in early stage

Table 1. Demographic information.

Cohort	Characteristics	Control	A+T+
A4	Age	69.65 ± 4.29	72.89 ± 4.80
	Gender(M/F)	23/32	115/153
ADNI	Age	73.14 ± 6.02	78.15 ± 6.58
	Gender(M/F)	95/129	78/81

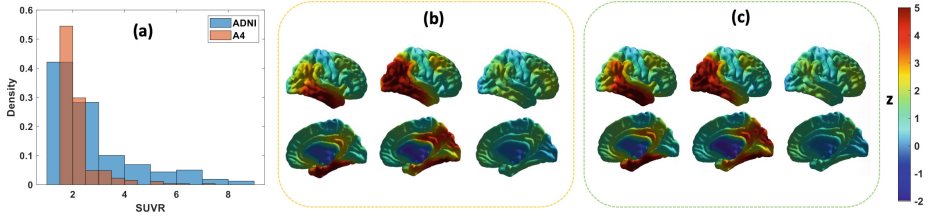


Fig. 5. Generalization results from our method. (a) Peak SUVR distributions of ADNI and A4. (b) Patterns of ADNI data based on model trained from the same cohort. (c) Patterns of ADNI data based on model trained from the A4 data.

and late stage show greater gaps for the SuStaIn method. This is caused by the unbalanced training samples across stages, as the SUVR of dominant A4 training data primarily concentrates on low intensity (Fig. 5(a)) and leads to insufficient training in late stages.

Table 2. Generalization performance measured by Rand index.

	Our method	SuStaIn
ADNI	0.8605	0.6648
A4	0.8957	0.8550

Generalization Performance Across Cohorts. The generalization performance of two methods was compared by the consistency of subtyping results of same data from models trained by different cohorts. For both methods, a model with three subtypes is first trained separately on ADNI and A4 data and then applied to both cohorts. Rand index [8] was used to measure the similarity of the subtyping results using different models and quantify the generalization.

Compared to the SuStaIn method, our method is more stable on both datasets as shown in Table 2. The inferior performance of the SuStaIn method is caused by the SUVR differences between cohorts as indicated in Fig. 5(a).

Table 3. Cognitive scores of ADNI subjects. (* denotes statistical significance ($P < 0.05$) with other subtypes.)

	Control	Subtype1	Subtype2	Subtype3
MMSE	29 ± 0.98	26.21 ± 3.55	26.02 ± 3.61	$27.84 \pm 3.38^*$
ADAS11	8.69 ± 2.78	15.35 ± 7.31	14.61 ± 6.67	$11.23 \pm 6.28^*$
ADAS13	12.39 ± 4.60	22.69 ± 10.12	21.98 ± 9.53	$16.70 \pm 8.77^*$

This is consistent with the results from the synthetic experiment where the SuStaIn method becomes unstable when the training A4 data has limited intensity range. Our method, however, focuses on the spreading patterns and is robust to intensity variations. The subtyping patterns of ADNI data with our models trained on both cohorts are shown in Fig. 5. Both results are consistent with the patterns derived from whole A+T+ samples in Fig. 4. Further evidence of the clinical relevance of the subtyping results from our method is indicated by the cognitive scores of ADNI subjects in Table 3. All subtypes show deviations from the normal control, and particularly subtype 3 is different from the other two subtypes with statistical significance ($P < 0.05$).

4 Conclusions

In the current study, we proposed a novel directed-graph-based framework with a new spatiotemporal pattern representation for parsing tau pathology heterogeneity and demonstrated its improved performance over the state-of-art SuStaIn method. Application of the proposed method on large-scale tau PET imaging datasets successfully demonstrated three subtypes with clear relevance to previously well-described clinical subtypes with distinct spatiotemporal patterns.

References

1. Blondel, V.D., Guillaume, J.L., Lambiotte, R., Lefebvre, E.: Fast unfolding of communities in large networks. *J. Stat. Mech. Theory Exp.* **2008**(10), P10008 (2008)
2. Braak, H., Braak, E.: Neuropathological staging of Alzheimer-related changes. *Acta Neuropathol.* **82**(4), 239–259 (1991)
3. Duff, I.S., Koster, J.: On algorithms for permuting large entries to the diagonal of a sparse matrix. *SIAM J. Matrix Anal. Appl.* **22**(4), 973–996 (2001)
4. Ferreira, D., Nordberg, A., Westman, E.: Biological subtypes of Alzheimer disease: a systematic review and meta-analysis. *Neurology* **94**(10), 436–448 (2020)
5. Fonteijn, H.M., et al.: An event-based model for disease progression and its application in familial Alzheimer’s disease and Huntington’s disease. *Neuroimage* **60**(3), 1880–1889 (2012)
6. Greve, D.N., et al.: Cortical surface-based analysis reduces bias and variance in kinetic modeling of brain pet data. *Neuroimage* **92**, 225–236 (2014)
7. Habes, M., Grothe, M.J., Tunc, B., McMillan, C., Wolk, D.A., Davatzikos, C.: Disentangling heterogeneity in Alzheimer’s disease and related dementias using data-driven methods. *Biol. Psychiat.* **88**(1), 70–82 (2020)
8. Hubert, L., Arabie, P.: Comparing partitions. *J. Classif.* **2**, 193–218 (1985)
9. Jack, C.R., Jr., et al.: Defining imaging biomarker cut points for brain aging and Alzheimer’s disease. *Alzheimer’s Dement.* **13**(3), 205–216 (2017)
10. Reeb, G.: Sur les points singuliers d’une forme de pfaff complètement intégrable ou d’une fonction numérique [on the singular points of a completely integrable pfaff form or of a numerical function], vol. 222, pp. 847–849 (1946)
11. Shi, Y., Lai, R., Toga, A.W.: Cortical surface reconstruction via unified Reeb analysis of geometric and topological outliers in magnetic resonance images. *IEEE Trans. Med. Imaging* **32**(3), 511–530 (2012)

12. Shi, Y., Li, J., Toga, A.W.: Persistent Reeb graph matching for fast brain search. In: Wu, G., Zhang, D., Zhou, L. (eds.) MLMI 2014. LNCS, vol. 8679, pp. 306–313. Springer, Cham (2014). https://doi.org/10.1007/978-3-319-10581-9_38
13. Sperling, R.A., et al.: The A4 study: stopping ad before symptoms begin? *Sci. Transl. Med.* **6**(228), 228fs13 (2014)
14. Ten Kate, M., et al.: Atrophy subtypes in prodromal Alzheimer’s disease are associated with cognitive decline. *Brain* **141**(12), 3443–3456 (2018)
15. Vogel, J.W., et al.: Four distinct trajectories of tau deposition identified in Alzheimer’s disease. *Nat. Med.* **27**(5), 871–881 (2021)
16. Whitwell, J.L., et al.: [18F] AV-1451 clustering of entorhinal and cortical uptake in Alzheimer’s disease. *Ann. Neurol.* **83**(2), 248–257 (2018)
17. Young, A.L., et al.: Uncovering the heterogeneity and temporal complexity of neurodegenerative diseases with subtype and stage inference. *Nat. Commun.* **9**(1), 1–16 (2018)